



Electrocatalytic decarboxylation of carboxylic acids over RuO₂ and Pt nanoparticles

Yang Qiu^{a,1,2}, Juan A. Lopez-Ruiz^{a,1,3}, Guomin Zhu^{b,c}, Mark H. Engelhard^d, Oliver Y. Gutiérrez^{b,*,4}, Jamie D. Holladay^{a,*,5}

^a Energy and Environment Directorate, Pacific Northwest National Laboratory, 902 Battelle Blvd., Richland, WA 99354, USA

^b Physical and Computational Sciences Directorate, Pacific Northwest National Laboratory, 902 Battelle Blvd., Richland, WA 99354, USA

^c Department of Materials Science and Engineering, University of Washington, Seattle, WA 98195, USA

^d Environmental Molecular Sciences Laboratory, Pacific Northwest National Laboratory, Richland, WA 99354, USA

ARTICLE INFO

Keywords:

Kolbe electrolysis
Electrocatalytic decarboxylation
Ruthenium oxide
Structure sensitivity
Valeric acid

ABSTRACT

We report electrocatalytic decarboxylation (ECDX) of valeric acid into paraffins, olefins, and alcohols via (non-) Kolbe electrolysis on electrodes with RuO₂ and Pt nanoparticles (NPs) as a greener alternative to thermocatalytic decarboxylation. The turnover frequency of ECDX increases, while the specific activity peaks as RuO₂ NP size increases. These opposing trends make the particle size of ~ 12 nm the optimum size for ECDX on RuO₂. Bulk Pt was active for ECDX, while Pt NPs were only active for the oxygen evolution reaction under our conditions. ECDX current efficiency remained constant in the studied potential range on RuO₂ NPs. Esterification was the favored reaction at 2.5 V vs. RHE; however, Kolbe electrolysis was the favored reaction at the expense of the esterification at 4.5 V vs. RHE. This work highlights the performance of nanostructured materials as an alternative to bulk materials as anodes for oxidative upgrading of carboxylic acids.

1. Introduction

As an abundant and renewable energy resource, biomass has been extensively studied for the production of biofuels and value-added chemicals [1–4]. During biomass valorization processes, deoxygenation pathways (e.g., dehydration, hydrogenation, decarboxylation, etc.) are necessary to reduce oxygen content from biomass-derived platform molecules [5,6]. Carboxylic acids are the main constituent of biomass-derived streams; however, their conversion via traditional thermo-catalytic routes (e.g., hydrodeoxygenation, decarboxylation, ketonization, etc.) require moderate temperatures (200–500 °C), moderate pressure (6–60 bar), and externally supplied H₂ [7–10]. For example, Lopez-Ruiz et al. reported the conversion of heptanoic acid to hexane at 300 °C and 40 bar over Pt/C and Pd/C [11]. Gosselink et al. performed the decarboxylation of stearic acid at 250 °C and 6 bar on Pd/carbon nanofiber [12].

Electrocatalytic upgrading may represent a more sustainable hydrogenation route compared to thermo-catalytic upgrading as it can be operated at ambient temperature and pressure without the need to supply H₂ [13]. Previous work has shown that electrocatalytic hydrogenation (ECH) can convert aldehydes, ketones, and phenolic compounds to their corresponding alcohols and alkanes over noble and base metals with even higher rates than thermocatalytic hydrogenation in some instances [14–21]. For example, Song et al. reported at least two orders of magnitude higher turnover frequency (TOF) of benzaldehyde ECH than benzaldehyde thermocatalytic hydrogenation [21]. However, ECH of carboxylic acids still remains a challenge at room temperature [15,17].

Our previous work showed that electrocatalytic decarboxylation (ECDX) is a viable route to upgrade carboxylic acids into olefins, paraffins, and alcohols at room temperature and atmospheric pressure without consuming H₂ via (non-)Kolbe electrolysis. The most accepted

* Corresponding authors.

E-mail addresses: oliver.gutierrez@pnnl.gov (O.Y. Gutiérrez), jamie.holladay@pnnl.gov (J.D. Holladay).

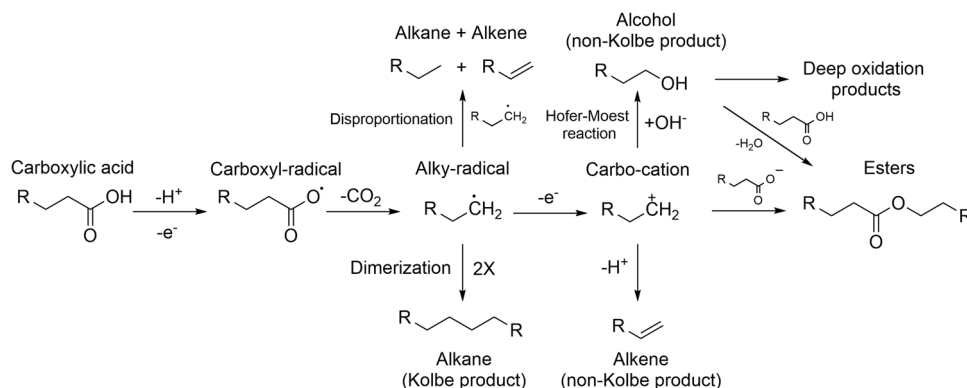
¹ Equal contributors.

² ORCID: 0000-0002-3190-3400.

³ ORCID: 0000-0002-9540-8070.

⁴ ORCID: 0000-0001-9163-4786.

⁵ ORCID: 0000-0001-5276-6882.



Scheme 1. Overview reaction mechanism for the formation of Kolbe products, non-Kolbe products, esters, and deep oxidation products. (Adapted from Levy et al. [25]).

mechanism of (non-)Kolbe electrolysis proceeds via the formation of radicals as illustrated in Scheme 1. The plausible roles of the electrode are to stabilize radical species and facilitate the transfer of charge carriers (i.e., OH^- , H^+ , and e^-) which aids the formation and cleavage of C—C bonds. After adsorption of carboxylic acid, a carboxyl-radical is generated through one-electron oxidation. The following decarboxylation leads to the formation of an alkyl-radical and CO_2 . On one hand, two alkyl-radicals can be dimerized into an alkane via Kolbe electrolysis, or disproportionated to a short alkane and a short alkene. On the other hand, the alkyl-radical can be further oxidized to carbocations with one electron transfer followed by deprotonation to yield an alkene via (non-)Kolbe electrolysis or reacting with water (or OH^-) to form an alcohol via the Hofer-Moest reaction. The alcohol reacts with a carboxylic acid to generate esters (reference experiments are described in the SI). Alternatively, esters can form upon the reaction between carbocations and deprotonated carboxylic acid anions. Alcohol further oxidizes to aldehydes, ketones, and carboxylic acids with shorter carbon chain (i.e., deep oxidation products) [22–24].

Studies of the (non-)Kolbe electrolysis has focused on bulk Pt materials (e.g., foil, mesh) because of their high selectivity to dimerized alkanes (Kolbe product) and better stability under the required potentials for Kolbe electrolysis (i.e., 2.1–2.8 V vs. NHE) than other bulk materials (e.g., C, Ni, Fe, etc.) [25–33]. However, our recent work demonstrated that a micro-scale RuO_2 thin film ($\text{RuO}_2\text{-TF}$) electrode has a comparable rate to that of a Pt foil for valeric acid (VA) ECDX at 4 V with a reversible hydrogen electrode (RHE) ($0.242 \text{ mmol}_{\text{VA}} \text{ h}^{-1} \text{ cm}^{-2}_{\text{geo}}$ and $0.316 \text{ mmol}_{\text{VA}} \text{ h}^{-1} \text{ cm}^{-2}_{\text{geo}}$, respectively) [34]. The measured ECDX TOFs were up to three orders of magnitude higher than the TOF for the comparable thermocatalytic decarboxylation at 300°C (14 s^{-1} and 0.0052 s^{-1} , respectively) [11,35]. Interestingly, micro-scale Pt thin film (Pt-TF) favored the competing oxygen evolution reaction (OER) showing negligible activity towards ECDX [34,36]. The reasons for the difference in ECDX activity were ascribed to structure sensitivity (e.g., particle size effect, surface composition change) which, to be best of our knowledge, remained unexplored for the ECDX reaction.

In this work, we deposited RuO_2 and Pt NPs on Ti electrodes and evaluated their performance for the ECDX of VA. Our results show that RuO_2 NPs have three orders of magnitude higher specific ECDX rate than bulk Pt foil and exhibit good stability against surface oxidation and morphology change during chronoamperometry tests. The ECDX TOF was found to increase with increasing RuO_2 particle size, and the maximum specific ECDX rate was obtained from RuO_2 NPs of 12.6 nm. Pt NPs had no apparent ECDX activity under the same reaction conditions regardless of the particle size, most likely due to the oxide layer formation. In contrast, all the Pt NPs were active for OER under the same potential to ECDX.

2. Experimental

2.1. Preparation of RuO_2 nanoparticles with different sizes

A 0.1 M Ru^{3+} solution was prepared by dissolving 0.01 mol $\text{RuCl}_3 \cdot x\text{H}_2\text{O}$ in 100 mL of deionized (DI) water. This solution was heated at 100°C for 10 min with vigorous stirring. One milliliter of 1.0 M NaOH solution was added to the Ru^{3+} solution to adjust the pH to ~ 10.5 and form $\text{Ru}(\text{OH})_x$ nuclei. This mixture was treated at 100°C for 60 min. After cooling, the mixture was centrifuged at 8000 rpm for 15 min. The obtained $\text{Ru}(\text{OH})_x$ NPs were washed with DI water (18.2 M Ω) to completely remove unreacted RuCl_3 , and dried at 60°C for 12 h [37].

Samples of 150 mg dried $\text{Ru}(\text{OH})_x$ NPs were calcinated at 200, 300, 500, and 700°C at a heating rate of 5°C min^{-1} under static air for 2 h. RuO_2 NPs with different particle sizes were obtained and named $\text{RuO}_2\text{-200}$, $\text{RuO}_2\text{-300}$, $\text{RuO}_2\text{-500}$, and $\text{RuO}_2\text{-700}$, according to the temperature of the treatment.

2.2. Preparation of Pt nanoparticles with different sizes

Commercial Pt NPs were treated in air at 100, 300, 350, and 400°C at a heating rate of $10^\circ\text{C min}^{-1}$ under 5 v/v% H_2/N_2 gas flowing at a rate of 100 mL min^{-1} for 1.0 (for 300°C) and 0.5 h (for 350 and 400°C). Pt NPs with different particle sizes were obtained and named Pt-100, Pt-300, Pt-350, and Pt-400.

2.3. Preparation of electrodes

The electrochemical characterizations were carried out in a sealed 120 mL glass cell with a three-electrode setup. A Pd foil and an Ag/AgCl electrode (Pine, LowProfile reference electrode) were used as the counter and reference electrodes, respectively. To fabricate the working electrode, a Pt catalyst ink ($15 \text{ mg}_{\text{Pt}} \text{ mL}^{-1}$) was prepared by mixing Pt NPs with 5 wt.% polytetrafluoroethylene (PTFE) solution (catalyst:PTFE = 95:5 w/w%) in DI water, while a RuO_2 catalysts ink ($15 \text{ mg RuO}_2 \text{ mL}^{-1}$) was prepared by dispersing RuO_2 in isopropyl alcohol, followed by sonication in a solution PTFE. We used a catalyst to PTFE weight ratio of 95:5. Ti foil was used as catalyst substrate due to its stability under the oxidation potential utilized in this work. A Ti foil ($2 \text{ cm} \times 2.5 \text{ cm} \times 1.27 \text{ mm}$) was etched in 10 w/v% oxalic acid at 90°C for 30 min. The treated Ti foil then was washed with DI water and air dried at room temperature. The as-prepared catalyst ink was sprayed on the treated Ti foil to achieve a final loading of $1.0 \text{ mg}_{\text{catalyst}} \text{ cm}^{-2}_{\text{geo}}$. After drying, $40 \mu\text{L}$ (20 μL per side) diluted 1 wt.% Nafion solution was drop-casted on the RuO_2 and Pt catalyst surfaces. The total geometric surface area of sprayed Pt or RuO_2 catalyst is 6 cm^2 (3 cm^2 per side).

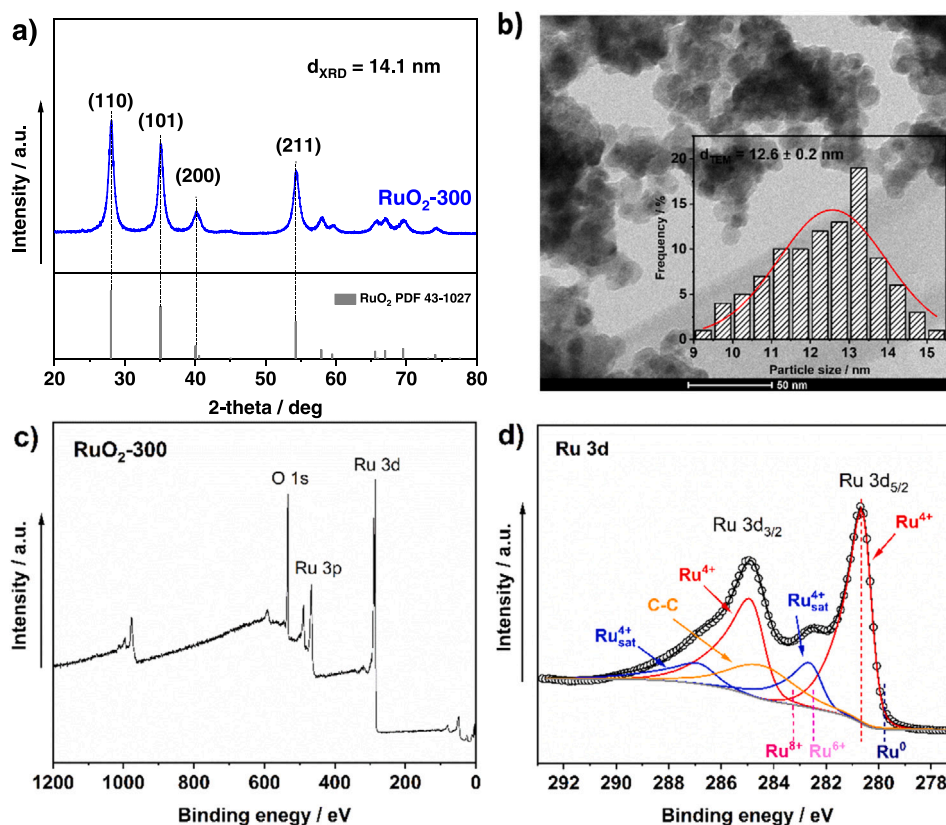


Fig. 1. a) XRD pattern, b) TEM image and size distribution of RuO₂-300 sample, c) XPS survey scanning spectrum, and d) Ru 3d high-resolution spectrum of RuO₂-300 sample. Physical characterization results for the Pt-300 sample can be found in Fig. S8.

2.4. Physicochemical characterization

Powder X-ray diffraction (XRD) patterns were obtained with a Rigaku MiniFlex II X-Ray Generator with monochromatic Cu K α radiation ($\lambda = 1.54056 \text{ \AA}$) at room temperature. The operating tube current and tube potential were 15 mA and 30 kV, respectively. Based on the XRD diffraction peak, we used the Debye–Scherrer formula shown in Eq. (1) to calculate the average crystalline sizes of Pt and RuO₂ NPs.

$$d = \frac{K \times \lambda}{B \times \cos[\frac{1}{2}\theta]} \quad (1)$$

the d is the average crystalline size of particles, K is the Scherrer constant of 0.94 for a spherical particle, B is the full width at half maximum of the specific XRD diffraction peaks in units of radian, λ is the X-ray wavelength (Cu K α average = 1.54178 \AA), and θ is the Bragg angle in radians [38].

An FEI Tecnai Scanning Transmission Electron Microscope was used to determine the morphology and particle size of the Pt and RuO₂ NPs. The compositions of the catalysts were analyzed by inductively coupled plasma optical emission spectroscopy. X-ray photoelectron spectroscopy (XPS) measurements were performed with a Physical Electronics Quantera Hybrid Scanning X-Ray Microprobe. This system uses a focused monochromatic Al K α X-ray (1486.7 eV) source for excitation and a spherical section analyzer. The instrument has a 32-element multichannel detection system. The X-ray beam is incident normal to the sample and the photoelectron detector is at 45° off-normal. High energy resolution spectra were collected using a pass-energy of 69.0 eV with a step size of 0.125 eV. For the Ag 3d_{5/2} line, these conditions produced a full width at half maximum of 0.92 eV \pm 0.05 eV. We used the Cu 2p_{3/2} feature at 932.62 \pm 0.05 eV and Au 4f_{7/2} at 83.96 \pm 0.05 eV to calibrate the binding energy scale.

2.5. Electrochemical characterization

The electrochemical characterization and reaction testing were described elsewhere [24]. The Ag/AgCl reference electrode was calibrated prior to ECDX tests in a single batch reactor. Two Pt wires and Ag/AgCl electrodes were used as the working, counter, and reference electrodes, respectively. The 0.14 M Na₂SO₄ solution (pH 6) was purged with ultrahigh-purity H₂ for at least 30 min before calibration to obtain H₂-saturated electrolyte, and the linear sweep voltammetry (LSV) test was conducted at a scan rate of 0.5 mV s⁻¹ from -0.55 to -0.45 V vs. Ag/AgCl to determine the thermodynamic potential for H₂ evolution and oxidation reaction (Fig. S1) [39]. We report all potentials against the RHE in this paper, which was converted from the potential vs. Ag/AgCl by using Eq. (2).

$$E_{\text{RHE}} = E_{\text{Ag/AgCl}} + 0.487 \text{ V} \quad (2)$$

The ECDX performance was investigated by CV, LSV, and chronoamperometry (i.e., constant potential) experiments using the BioLogic (SP-150). CV and LSV tests were performed in 0.14 M Na₂SO₄ solution with and without 0.5 M VA. The electrolyte was purged with N₂ at 100 mL min⁻¹ for at least 30 min to remove dissolved O₂. The polarization curves were subsequently collected with scanning rate of 50 mV s⁻¹ ranging between 1.2 and 2.8 V vs. RHE with iR correction.

Electrochemical impedance spectroscopy was conducted by applying alternating current voltage with 10 mV amplitude at frequencies ranging from 300 kHz to 100 mHz. A Nyquist plot was obtained at open circuit voltage, and the measured solution resistance, R_s , was used to correct the practical potential applied on the working electrode using Eq. (3).

$$E_{\text{iR-corrected}} = E_{\text{applied}} - iR_s \quad (3)$$

In Eq. (3), E_{applied} is the applied potential on the working electrode (i.

Table 1

Summary of electrode characterization results as a function of synthesis temperature. The average particle diameter determined from TEM is d_{TEM} , d_{XRD} is the average crystallite size determined by the Debye–Scherrer equation, SSA_{TEM} is the metal surface area calculated from d_{TEM} , and electrochemical surface area (ECSA) is the electrochemical surface area measured using impedance and the hydrogen underpotential deposition method.

Samples	$d_{\text{TEM}}^*/\text{nm}$	$\text{SSA}_{\text{TEM}}/\text{m}^2/\text{g}_{\text{catalysts}}^{-1}$	d_{XRD}/nm	$\text{ECSA}/\text{m}^2/\text{g}_{\text{catalysts}}^{-1}$
RuO ₂ -200	9.3 ± 0.1	92.6	9.1	59.1
RuO ₂ -300	12.6 ± 0.2	68.3	14.1	36.8
RuO ₂ -500	20.1 ± 0.2	42.8	22.9	26.2
RuO ₂ -700	37.8 ± 0.7	22.7	42.3	12.7
Pt-100	5.0 ± 0.1	55.9	6.8	31.6
Pt-300	10.2 ± 0.0	27.4	12.8	18.7
Pt-350	17.9 ± 0.2	15.6	20.6	12.6
Pt-400	44.5 ± 1.4	6.30	50.1	7.70

*TEM images with size distributions of RuO₂ and Pt NPs are shown in Fig. S3 and S5; Cyclic voltammograms of RuO₂ and Pt NPs for ECSA measurement are shown in Fig. S4 and S6; XRD patterns of RuO₂ and Pt NPs are shown in Fig. S7.

e., the anode in this work), i is the corresponding measured current, R_s is the compensated (85%) electrolyte resistance determined by electrochemical impedance spectroscopy, and $E_{\text{iR-corrected}}$ is the potential after iR correction [40].

The chronoamperometry was conducted in 0.5 M VA + 0.14 M Na₂SO₄ solution that was purged using N₂ flowing at 100 mL min^{−1} for at least 30 min prior to each test. Constant potentials of 2.5, 3.5, and 4.5 V vs. RHE were applied for 1–6 h. The electrolyte was maintained at ~ 0 °C and ambient pressure during the reaction, and N₂ gas flowing at 20 mL min^{−1} carried gas products (e.g., butene, propylene, CO₂, etc.) to an online gas chromatography (Inficon Micro GC Fusion® Gas

Analyzer equipped with a thermal conductivity detector) instrument. A trapping system containing isopropyl alcohol at ~ 0 °C was used to collect volatile compounds (e.g., octane, butanol, etc.). A 20 mL volume of dichloromethane was added to the electrolyte after chronoamperometry test to extract octane and esters. All aqueous products in both the aqueous and organic phases were quantified using a combination of high-performance liquid chromatography (equipped with a Waters 2414 refractive index detector) and an offline GC (Agilent 6890 equipped with a flame ionization detector), which has been reported in our previous work [34].

3. Results and discussion

3.1. Materials physical characterizations

RuO₂ NPs were synthesized through precipitation of Ru(OH)_x at pH 10.5 from RuCl₃ solutions, followed by calcination in air at 300 °C (RuO₂-300). A detailed description of the synthesis protocol can be found the experimental section. The x-ray diffractogram of the Ru(OH)_x sample showed a broad peak centered at ~ 33.0° (Fig. S2). The diffractogram of RuO₂-300 had three major diffraction peaks corresponding to rutile RuO₂ (110), (101), and (211) facets at 28.0°, 35.1°, 54.3°, respectively (Fig. 1a) [41]. The average size of RuO₂ NPs in RuO₂-300 (i.e., an electrode composed of RuO₂ NP calcined at 300 °C) sample were determined using both the Debye–Scherrer equation (d_{XRD}) and transmission electron microscopy (TEM) (d_{TEM}) as shown in Table 1 (the particle size distribution is shown in Fig. 1b).

The particle size derived from the TEM analysis and the crystal size derived from X-ray diffraction (XRD) are in good agreement (i.e., 12.6 nm and 14.1 nm, respectively) [42]. XPS was used to determine the surface composition and oxidation state of Ru in RuO₂-300. The survey spectrum (Fig. 1c) shows only Ru and O elements, indicating that Cl[−] from the Ru precursor was completely removed. The high-resolution Ru 3d spectrum (Fig. 1d) shows two major peaks that were deconvoluted

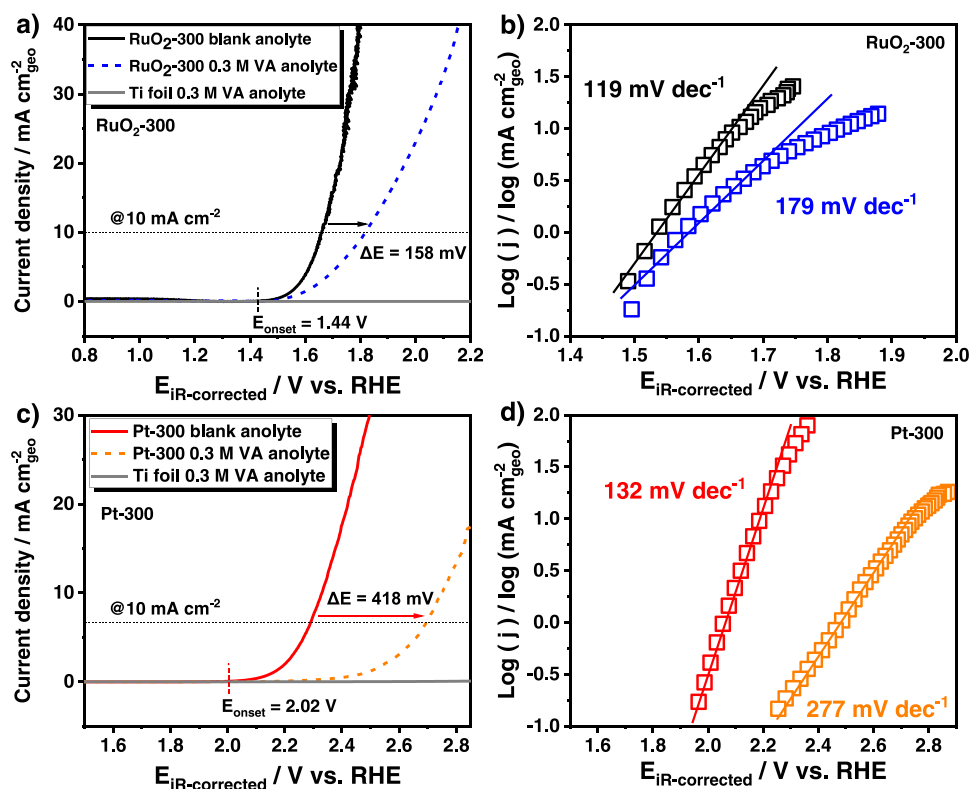


Fig. 2. a, c) Linear sweep voltammogram and b, d) corresponding Tafel plots measured on RuO₂-300 and Pt-300 in N₂-saturated 0.14 M Na₂SO₄ solution with and without 0.3 M VA (pH 6), collected at 50 mV s^{−1}. More information regarding the onset potentials and Tafel slope can be found in Table S1.

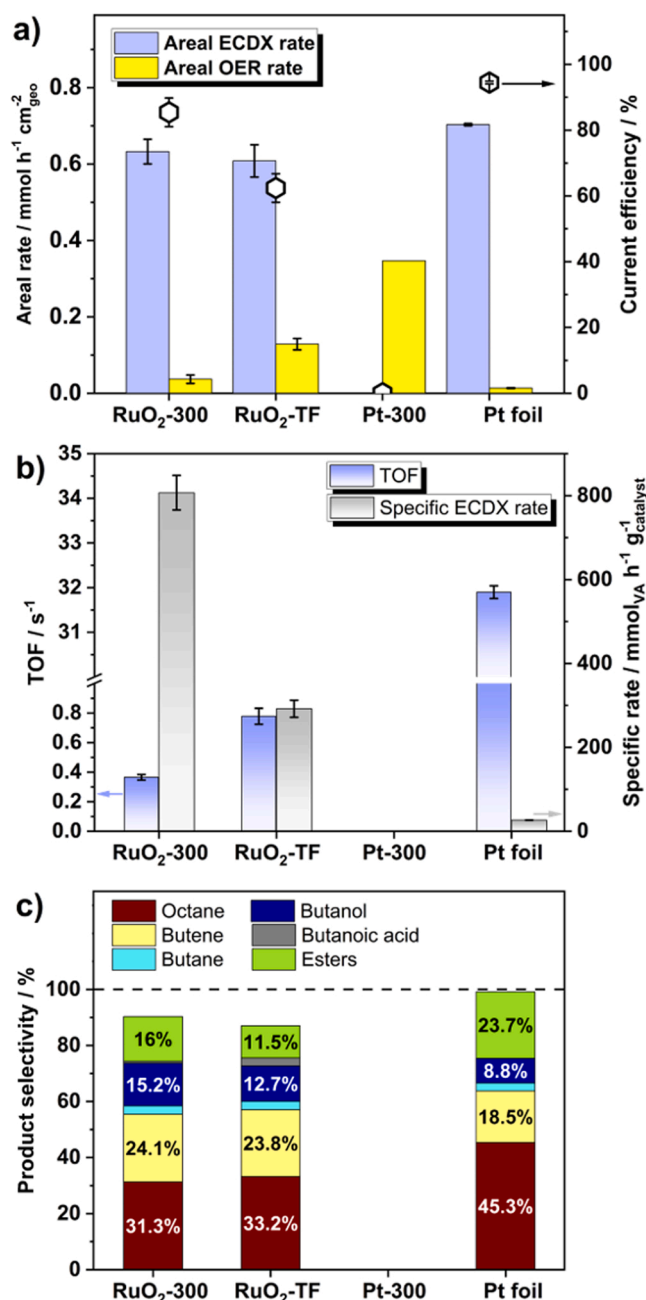


Fig. 3. a) Areal ECDX and OER rate; b) TOF and specific rate of ECDX; and c) product selectivity of valeric acid ECDX for 1 h over RuO₂-300, RuO₂-TF, Pt-300, and Pt foil electrodes at constant anodic potential of 4.5 V vs. RHE. Reaction conditions: 70 mL of 0.5 M valeric acid + 0.14 M Na₂SO₄ solution (pH 6) at ~0 °C. The complete product distribution can be found in Table S3.

into the peaks of Ru⁴⁺ 3d_{5/2} (280.5 eV), Ru⁴⁺ 3d_{3/2} (284.7 eV), Ru_{sat}⁴⁺ 3d_{5/2} (282.5 eV), and Ru_{sat}⁴⁺ 3d_{3/2} (286.7 eV) [38,43]. The lack of Ru⁶⁺ 3d (282.9/287.1 eV) and Ru⁸⁺ 3d (283.3/287.5 eV) peaks and their corresponding sat peaks (e.g., Ru_{sat}⁶⁺ 3d_{3/2} of 288.7 eV, Ru_{sat}⁸⁺ 3d_{3/2} of 289.3 eV, etc.) suggests that only Ru⁴⁺ is present in our sample. A carbon signal (284.8 eV) with a C-C structure was observed and overlapped with Ru 3d peaks. This signal is attributed to adventitious carbon.

Pt NPs also were prepared through heat treatment at 300 °C of the impregnated plate. As shown in Fig. S8a and S8b, Pt-300 exhibited an average size of 10.2 nm with a broad size distribution of 7–16 nm, which is in good agreement with the 12.8 nm size derived from XRD. The XPS survey scanning and Pt 4f high-resolution spectra (Fig. S8c and S8d)

show that the metallic Pt is predominant in Pt-300 samples, and the concentrations of Pt⁰ and Pt²⁺ (and Pt⁴⁺) were 94.5 at% and 5.5 at%, respectively.

The specific surface area (SSA) and electrochemical surface area (ECSA) of RuO₂-300 and Pt-300 are listed in Table 1 (see supporting information for SSA and ECSA calculations) [44]. Although Pt-300 and RuO₂-300 electrodes have similar average particle sizes and size distributions, the higher density of Pt (21.45 g_{Pt} cm⁻³) compared to that of RuO₂ (6.97 g_{RuO2} cm⁻³) leads a smaller SSA and ECSA for Pt (SSA of 27.4 m² g_{Pt}⁻¹, ECSA of 18.7 m² g_{Pt}⁻¹) than for RuO₂ (SSA of 68.3 m² g_{RuO2}⁻¹, ECSA of 36.8 m² g_{RuO2}⁻¹). As a result, a ~50% lower RuO₂ loading is required to achieve the same ECSA and active sites as the Pt electrodes, which is an important advantage for nanoscale RuO₂ as the alternative electrocatalyst to Pt materials.

3.2. Electrocatalytic decarboxylation of valeric acid

Following the experimental protocols outlined in our previous work with RuO₂-TF and Pt-TF for VA ECDX, the electrode performance for VA ECDX was evaluated preliminarily using a rotating disk electrode [34]. The onset potential, Tafel slope, and required potential for current density of 10 mA cm⁻²_{geo} were collected and summarized in Table S1. RuO₂-300 exhibited a well-defined OER polarization curve (in the absence of organic compounds) in 0.14 M Na₂SO₄ solution (pH 6) with an onset potential of 1.44 V vs. RHE and a Tafel slope of 119 mV dec⁻¹ (Fig. 2a and b).

This Tafel slope is higher than the previously reported Tafel slope of 40–50 mV dec⁻¹ over RuO₂-based catalysts in strong acidic media (0.5 M H₂SO₄ with pH ~ 0), indicating low OER activity in our weakly acidic conditions [40,45]. Pt-300 showed a higher onset potential of 2.02 V vs. RHE with a larger Tafel slope of 132 mV dec⁻¹ than RuO₂-300, suggesting Pt-300 has inferior OER activity under identical conditions. When VA was added into electrolyte, the Tafel slope increased for both RuO₂-300 and Pt-300 to 179 and 277 mV dec⁻¹, respectively. The potential required to achieve 10 mA cm⁻²_{geo} also increased for RuO₂-300 and Pt-300 to ΔE_{10mAcm-2} = 158 mV and 418 mV, respectively (Fig. 2). These changes imply that the adsorption of VA-derived intermediate (i.e., valerate) suppresses OER on both the RuO₂-300 and the Pt-300 electrode [46]. The ECDX activity over RuO₂-300 and Pt-300 was studied through chronoamperometry tests in 0.5 M VA + 0.14 M Na₂SO₄ solution (pH 6) at 4.5 V vs. RHE. We have demonstrated in our previous work that the applied potential controls ECDX activity, current efficiency (CE), and corresponding product selectivity on RuO₂-TF and (bulk) Pt foil electrodes [24]. To minimize the formation of deep oxidation products on Pt, and mitigate the competing OER, ECDX was performed at constant potential of 4.5 V vs. RHE and at 0 °C for 1 h. RuO₂-TF and Pt foil also were investigated under the same conditions (the ECSA of RuO₂-TF and Pt foil are given in the supporting information, Table S2).

RuO₂-300 (0.60 mmol_{VA} h⁻¹ cm⁻²_{geo}), RuO₂-TF (0.57 mmol_{VA} h⁻¹ cm⁻²_{geo}), and Pt foil (0.70 mmol_{VA} h⁻¹ cm⁻²_{geo}) showed similar areal ECDX rates (Fig. 3a), but different areal OER rates. RuO₂-300 (0.048 mmol_{O2} h⁻¹ cm⁻²_{geo}) and RuO₂-TF (0.143 mmol_{O2} h⁻¹ cm⁻²_{geo}) exhibited higher areal OER rate than Pt foil (0.014 mmol_{O2} h⁻¹ cm⁻²_{geo}). This led to the CE trend of Pt foil (94.5%) > RuO₂-300 (85.4%) > RuO₂-TF (62.4%); that is, ECDX is preferred over OER on RuO₂-300 and Pt foil. In contrast, Pt-300 favored OER making ECDX of VA negligible, which is consistent with our previous results showing that ECDX is negligible on Pt microstructures (Pt-TF) [24]. This result suggests that the change in onset potential and Tafel slope observed on Pt-300 in the presence of VA is not associated with a change in preferred reaction from OER to ECDX, but to the suppression of OER in the presence of VA. We hypothesize that the differences in ECDX performance between nanoscale Pt-300 and bulk Pt foil is due to different oxidation states of NPs and bulk Pt under the same potential of 4.5 V vs. RHE. Verifying this hypothesis, we observed a change in Pt⁰/Pt²⁺+Pt⁴⁺ ratio

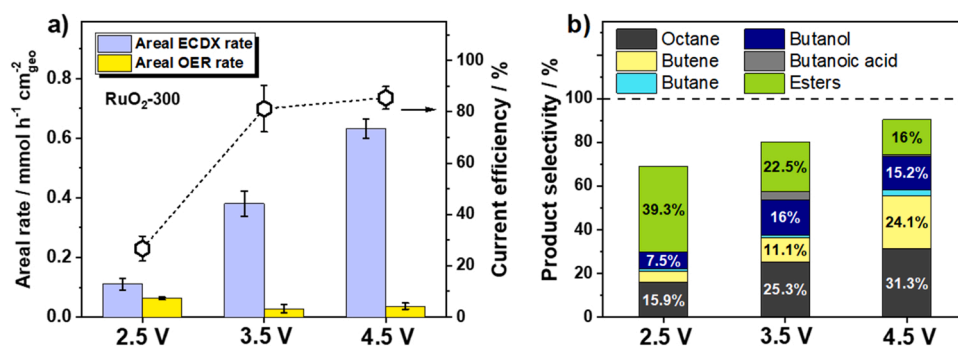


Fig. 4. a) Areal ECDX and OER rate, and b) product selectivity of valeric acid (VA) ECDX over RuO₂-300 electrode at constant potential of 2.5, 3.5, and 4.5 V vs. RHE for 1 h. Reaction conditions: 70 mL of 0.5 M VA + 0.14 M Na₂SO₄ solution (pH 6) at ~ 0 °C. The complete product distribution can be found in Table S4.

from 94.5 at.%/5.5–76.1 a.t%/23.9 at.% for Pt-300 before and after the ECDX tests (Fig. S8d and S4), suggesting the formation of oxide layers on Pt NPs. This is consistent with previous reports showing that Pt NPs oxidize more easily than (bulk) Pt foil because of the higher oxophilicity of Pt NPs [47,48]. Damjanovic et al. demonstrated that the OER activity exponentially decreases with an increase in the Pt oxide layer thickness [47,49]. We investigated the effect of the oxide layer formation on the ECDX activity over Pt-300 and Pt foil by conducting a 100 cycles of cyclic voltammetry (CV) scanning in 0.14 M Na₂SO₄ with and without 0.5 M VA. As shown in Fig. S10, the OER current density decreased by 52% and 10% on Pt-300 and Pt foil, respectively, after 100 cycles scanning in blank 0.14 M Na₂SO₄ solution, which suggests a faster oxide layer formation on Pt-300 than Pt foil. When VA was introduced, the measured current density decreased by 43% on Pt-300 but by less than 2% on Pt foil after 100 cycles scanning. We speculate that the presence of VA on Pt foil suppresses OER and prevents the Pt foil surface from oxidation, which is supported by the negligible current density change and lack of oxide formation in the presence of VA. However, the formation of a surface PtO_x layer on the Pt NPs is very facile and is not suppressed in the presence of VA. As shown in Fig. 3a, the PtO_x layer formed on the Pt NPs is not active for ECDX but remains active for OER. It should be noted that both RuO₂-300 and Pt-300 were synthesized in the same particle size range using Nafion as binder but only the RuO₂ NPs were active for ECDX, suggesting that the presence of Nafion is not responsible for the lack of ECDX activity with Pt NPs. This is supported by the fact that we synthesized a Nafion-free Pt electrode in our previous work that was also inactive for VA ECDX [34].

The ECDX activity was evaluated by normalizing reaction rates to the mass of catalytic material (i.e., specific rate) and to the number of active sites (i.e., TOF) as summarized in Fig. 3b. Despite the lower ECDX TOF on RuO₂-300 than on Pt foil and RuO₂-TF, RuO₂-300 showed 35 and 2 times higher specific rates than Pt foil and RuO₂-TF, respectively. In addition, RuO₂-300 exhibited similar (non-)Kolbe product selectivity to RuO₂-TF (Fig. 3c), indicating that the RuO₂ morphology and particle size did not noticeably affect ECDX product selectivity. Compared to Pt foil, both RuO₂-300 and RuO₂-TF showed lower octane and ester selectivities and higher butene and butanol selectivities (Fig. 3c), which is in good agreement with our previous results [34].

With a higher specific rate and CE, the RuO₂ NPs represent a better low metal loading catalyst than Pt NPs, RuO₂-TF and Pt-TF for the ECDX reaction. Therefore, we investigated the effect of applied potential on the ECDX activity and product selectivity. When the potential decreases from 4.5 to 2.5 V vs. RHE, the ECDX rate decreased by a factor of ~ 6 (from 0.60 to 0.09 mmol_{VA} h⁻¹ cm⁻² geo), while the OER rate increased by 40% (from 0.048 to 0.067 mmol_{O₂} h⁻¹ cm⁻² geo) (Fig. 4a). The selectivity of both Kolbe (i.e., octane, from 31.3% to 15.9%) and non-Kolbe products (e.g., butene, from 24.1% to 5.20%; butanol, from 15.2% to 7.50%; etc.) decreased, while the ester selectivity increased from 16.0% to 39.3% (Fig. 4b).

These results suggest that esterification and alcohol formation via

(non-)Kolbe electrolysis are favored at low potentials, while paraffin and olefin formation via Kolbe and (non-)Kolbe electrolysis are favored at higher potentials. Surprisingly, the overall selectivity towards alcohol formation (i.e., alcohol + esterification) remained similar regardless of the applied potential. For example, at 2.5 V vs. RHE the overall alcohol selectivity was 27.5% (7.50% direct alcohol + 20.0% from ester), while at 4.5 V vs. RHE the overall alcohol selectivity was 28% (16.0% direct alcohol + 12.0% from ester). Overall, the nanoscale RuO₂-300 is more active than RuO₂-TF toward ECDX, and a lower catalyst loading of RuO₂ is required to achieve the same ECDX performance with similar products selectivity to Pt foil.

We also investigated the RuO₂ NP's stability (composition) and corresponding electrode durability (i.e., performance over operation time). As shown in Fig. S11a and S11b, RuO₂-300 exhibited similar Ru 3d spectra before and after 6 h of ECDX chronoamperometry tests at 4.5 V vs. RHE. Only Ru⁴⁺ 3d peaks were observed in the XPS spectra of the used RuO₂-300. Signals assignable to Ru⁶⁺ and Ru⁸⁺ (i.e., RuO₃ and RuO₄ respectively) were not observed, suggesting that as-synthesized RuO₂ is stable even when operating at 4.5 V vs. RHE. Inductively coupled plasma optical emission spectroscopy (Optima 7000 DV, PerkinElmer) results show that < 1 ppm Ru was found in the electrolyte (i.e., < 1.2% of the total Ru loading) after 6 h ECDX tests, further demonstrating the good stability of RuO₂ NPs on the electrode. Based on the TEM results, the average particle size increased from 12.6 to 14.0 nm as shown in Fig. S11c. However, the RuO₂-300 exhibited stable areal ECDX rates of ~ 0.4 mmol_{VA} h⁻¹ cm⁻² geo during the 6 h-test (Fig. S12a). The electrode durability was studied further by reproducing the ECDX activity in three different one-hour chronopotentiometry tests. As shown in Fig. S12b, there were no significant changes in the ECDX and OER rates or the CE. Overall, the results of both the physical and electrochemical characterizations demonstrated good RuO₂-300 stability and electrode durability under the reaction conditions studied.

3.3. Effect of RuO₂ and Pt nanoparticle sizes on VA ECDX performance

To assess the structure sensitivity of the RuO₂ and Pt for the ECDX reaction, RuO₂ and Pt NPs with different particle sizes were prepared through calcination at different temperatures. The ECSA and average particle size of RuO₂ and Pt NPs are summarized in Table 1. As expected, the ECSA decreased as the temperature of the thermal treatment increased for both the RuO₂ and Pt electrodes. Because Pt is denser than RuO₂, a smaller ECSA was measured from Pt NPs that have similar particle sizes as the RuO₂ NPs.

The ECDX activity of all the RuO₂ and Pt electrodes was studied via bulk chronoamperometry in 0.5 M VA + 0.14 M Na₂SO₄ solution (pH 6) at 4.5 V vs. RHE for 1 h. As shown in Fig. 5a, the nanoscale RuO₂ electrodes exhibited similar areal ECDX rates (0.60 mmol_{VA} h⁻¹ cm⁻² RuO₂) but different OER rates to that of RuO₂-TF. As the average NP size increased from 9.3 to 12.6 nm, the areal OER rate decreased ~ 3 times from 0.15 to 0.05 mmol_{O₂} h⁻¹ cm⁻² RuO₂. RuO₂ NPs with average

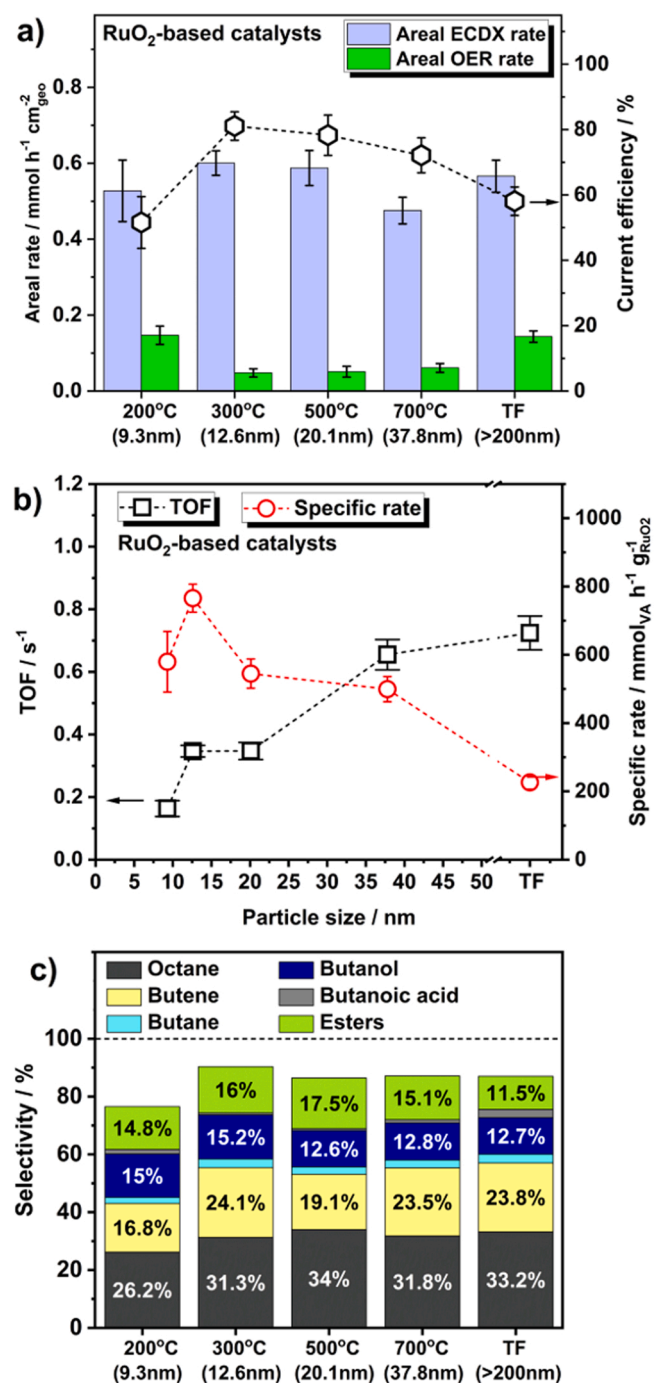


Fig. 5. a) Areal ECDX and OER rates; b) TOF and specific rate, and c) product selectivity of valeric acid (VA) ECDX for 1 h over RuO₂-200, 300, 500, 700 and RuO₂-TF electrodes, at a constant potential of 4.5 V vs. RHE. Reaction conditions: 70 mL of 0.5 M VA + 0.14 M Na₂SO₄ solution (pH 6) at ~0 °C. The complete product distribution can be found in Table S5.

sizes ranging between 12.6 and 20.1 nm had a similar areal OER ($\sim 0.05 \text{ mmol O}_2 \text{ h}^{-1} \text{ cm}^{-2}_{\text{RuO}_2}$), but the rate increased by ≈ 3 times with RuO₂ NPs sizes > 200 nm (RuO₂-TF, $0.14 \text{ mmol O}_2 \text{ h}^{-1} \text{ cm}^{-2}_{\text{RuO}_2}$).

These changes in areal OER rate as a function of RuO₂ particle size could not be correlated with changes in ECSA. As shown in Table S6, the OER rate normalized by ECSA also changes with particle size suggesting that OER on RuO₂ also is structure sensitive. Consequently, the maximum CE of 81.1% was obtained from RuO₂-300 (12.6 nm), followed by CE decreasing to 58.1% (RuO₂-TF) as the RuO₂ particle size increased further. The intrinsic ECDX activity was evaluated by

determining TOF (normalized by the number active sites) and specific rate (normalized by catalyst mass) (Fig. 5b). The ECDX TOF monotonically increased with particle size increasing from 9.3 (RuO₂-200) to > 200 nm (TF). The maximum specific rate was obtained from RuO₂-300 with a 12.6 nm particle size, while the ECDX specific rate decreased as the RuO₂ NP size increased. Interestingly, all RuO₂ NP electrodes exhibited product distributions similar to those of RuO₂-TFs (Fig. 5c), emphasizing that selectivity is not structure-sensitive, while the ECDX and OER rates are structure-sensitive (i.e., they are affected by the particle size).

On the other hand, all nanoscale Pt samples favored OER. The areal OER rates decreased (from 0.38 to $0.10 \text{ mmol O}_2 \text{ h}^{-1} \text{ cm}^{-2}_{\text{geo}}$) with Pt particle size increasing from 5.0 to 44.5 nm (Fig. S13 and Table S6). In contrast, bulk Pt foil favored ECDX with the high CE of 94.0%. The OER rate normalized by the ECSA shows that all the Pt NPs have > 7 times lower OER activity than the bulk Pt foil, even when the bulk Pt foil operated at 94.0% CE (i.e., 6.0% of the current was going towards OER) (Table S6). This result suggests that the formation of the PtO_x layer on the Pt NPs hinders both ECDX and OER rates regardless of the average Pt particle size change. Therefore, Pt NPs cannot be used as the electrocatalyst for ECDX in biomass upgrading.

4. Conclusions

We synthesized and evaluated nanoscale RuO₂ and Pt particles for the electrocatalytic decarboxylation (ECDX) of valeric acid (VA) in aqueous solution at room temperature and ambient pressure. The ECDX activity (e.g., areal ECDX rate, specific rate), current efficiency (CE), and (non-)Kolbe product selectivity was evaluated through chronoamperometry tests at 4.5 V vs. RHE. A RuO₂-based electrode (RuO₂-300) composed of 12.6 nm nanoparticles (NPs) exhibited three orders of magnitude higher ECDX specific rate and areal ECDX rate similar to Pt foil. In addition, RuO₂-300 NPs showed good stability with robust electrode durability during 6 h chronoamperometry test without apparent change in surface composition nor particle agglomeration. In contrast, while bulk Pt foil was active for ECDX, the 5 to 44.5 nm Pt NPs synthesized in this work only catalyzed OER. The inhibition of ECDX and decrease of OER rate on Pt NPs were attributed to the formation of Pt oxide.

We found the turnover frequency (TOF) of ECDX increases with RuO₂ particle size, while the specific activity decreases as RuO₂ particle size decreases. However, similar (non-)Kolbe product selectivity was observed for all the nanoscale RuO₂ electrodes. These results suggest that the ECDX rates is structure-sensitive while the product selectivity is structure-insensitive. RuO₂ NPs favored (non-)Kolbe products (i.e., butane, butene, butanol, and butanoic acid, etc.), while the Kolbe product (i.e., octane) was favored on Pt foil. The ECDX performance of the RuO₂-300 also is potential-dependent. The ECDX and OER rates and selectivity to Kolbe products increase as the potential increases. At 2.5 V vs. RHE, RuO₂ NPs were selective toward esterification products, but at 4.5 V vs. RHE, the Kolbe selectivity increases at the expense of the esterification selectivity.

Overall, this work shows how nanoscale RuO₂ electrodes are stable for the ECDX reaction and can achieve activity similar to that of bulk electrodes at a fraction of the metal loading. Compared to Pt, RuO₂ NPs are a more suitable electrode material for the development of active, lower cost electrodes for the ECDX reaction. Further, the electrode synthesis, testing, and characterization approach outlined in this work provides guidance for studies focused on evaluating the anodic electrocatalytic valorization of biomass-derived molecules.

CRediT authorship contribution statement

Yang Qiu: Methodology, Investigation, Data analysis, Writing – original draft. **Juan A. Lopez-Ruiz:** Data curation, Conceptualization, Writing – review & editing. **Guomin Zhu:** Methodology,

Experimentation. **Mark H. Engelhard**: Experimentation, Data curation. **Oliver Y. Gutiérrez**: Supervision, Funding acquisition, Writing – review & editing. **Jamie D. Holladay**: Conceptualization, Supervision, Funding acquisition.

Declaration of Competing Interest

The authors declare that they have no known competing financial interests or personal relationships that could have appeared to influence the work reported in this paper.

Acknowledgements

The research described in this paper was undertaken under the Chemical Transformation Initiative at Pacific Northwest National Laboratory (PNNL) conducted under PNNL's Laboratory Directed Research and Development Program. PNNL is a U.S. Department of Energy (DOE) Office of Science national laboratory located in Richland, Washington. O.Y.G. would like to acknowledge support by the U.S. DOE, Office of Basic Energy Sciences, Division of Chemical Sciences, Geosciences, and Biosciences (FWP 47319). We gratefully acknowledge Teresa Lemmon and Marie Swita at PNNL for their help with the sample analysis and ICP tests. XPS characterizations were conducted in the Environmental Molecular Sciences Laboratory (Grid.436923.9), a DOE Office of Science user facility sponsored by the Office of Biological and Environmental Research.

Appendix A. Supporting information

Supplementary data associated with this article can be found in the online version at [doi:10.1016/j.apcatb.2021.121060](https://doi.org/10.1016/j.apcatb.2021.121060).

References

- [1] S. Chu, A. Majumdar, Opportunities and challenges for a sustainable energy future, *Nature* 488 (2012) 294–303, <https://doi.org/10.1038/nature11475>.
- [2] A.J. Ragauskas, C.K. Williams, B.H. Davison, G. Britovsek, J. Cairney, C.A. Eckert, W.J. Frederick, J.P. Hallett, D.J. Leak, C.L. Liotta, J.R. Mielenz, R. Murphy, R. Templer, T. Tschaplinski, The path forward for biofuels and biomaterials, *Science* 311 (2006) 484–489, <https://doi.org/10.1126/science.1114736>.
- [3] E.L. Kunkes, D.A. Simonetti, R.M. West, J.C. Serrano-Ruiz, C.A. Gartner, J. A. Dumesic, Catalytic conversion of biomass to monofunctional hydrocarbons and targeted liquid-fuel classes, *Science* 322 (2008) 417–421, <https://doi.org/10.1126/science.1159210>.
- [4] J.C. Serrano-Ruiz, R. Luque, A. Sepulveda-Escribano, Transformations of biomass-derived platform molecules: from high added-value chemicals to fuels via aqueous-phase processing, *Chem. Soc. Rev.* 40 (2011) 5266–5281, <https://doi.org/10.1039/C1CS15131B>.
- [5] H. Wang, S.J. Lee, M.V. Olarte, A.H. Zacher, Bio-oil stabilization by hydrogenation over reduced metal catalysts at low temperature, *ACS Sustain. Chem. Eng.* 4 (2016) 5533–5545, <https://doi.org/10.1021/acssuschemeng.6b01270>.
- [6] J.A. Ramirez, R.J. Brown, T.J. Rainey, A review of hydrothermal liquefaction bio-crude properties and prospects for upgrading to transportation fuels, *Energies* 8 (2015) 6765–6794, <https://doi.org/10.3390/en8076765>.
- [7] M. Sadakiyo, S. Hata, T. Fukushima, G. Juhasz, M. Yamauchi, Electrochemical hydrogenation of (non)-aromatic carboxylic acid derivatives as a sustainable synthesis process: from catalyst design to device construction, *Phys. Chem. Phys.* 21 (2019) 5882–5889, <https://doi.org/10.1039/C8CP07445C>.
- [8] H. Olcay, L.J. Xu, Y. Xu, G.W. Huber, Aqueous-phase hydrogenation of acetic acid over transition metal catalysts, *Chemcatchem* 2 (2010) 1420–1424, <https://doi.org/10.1002/cctc.201000134>.
- [9] J. Ullrich, B. Breit, Selective hydrogenation of carboxylic acids to alcohols or alkanes employing a heterogeneous catalyst, *ACS Catal.* 8 (2018) 785–789, <https://doi.org/10.1021/acscatal.7b03484>.
- [10] J.A. Lopez-Ruiz, A.R. Cooper, G.S. Li, K.O. Albrecht, Enhanced hydrothermal stability and catalytic activity of La₂Zr₂O₇ mixed oxides for the ketonization of acetic acid in the aqueous condensed phase, *ACS Catal.* 7 (2017) 6400–6412, <https://doi.org/10.1021/acscatal.7b01071>.
- [11] J.A. Lopez-Ruiz, H.N. Pham, A.K. Datye, R.J. Davis, Reactivity and stability of supported Pd nanoparticles during the liquid-phase and gas-phase decarbonylation of heptanoic acid, *Appl. Catal. A-Gen.* 504 (2015) 295–307, <https://doi.org/10.1016/j.apcata.2015.01.032>.
- [12] R.W. Gosselink, W. Xia, M. Muhler, K.P. De Jong, J.H. Bitter, Enhancing the activity of Pd on carbon nanofibers for deoxygenation of amphiphilic fatty acid molecules through support polarity, *ACS Catal.* 3 (2013) 2397–2402, <https://doi.org/10.1021/cs400478q>.
- [13] L. Du, Y.Y. Shao, J.M. Sun, G.P. Yin, C.Y. Du, Y. Wang, Electrocatalytic valorization of biomass derived chemicals, *Catal. Sci. Technol.* 8 (2018) 3216–3232, <https://doi.org/10.1039/C8CY00533H>.
- [14] S.K. Green, G.A. Tompsett, H.J. Kim, W.B. Kim, G.W. Huber, Electrocatalytic reduction of acetone in a proton-exchange-membrane reactor: a model reaction for the electrocatalytic reduction of biomass, *Chemsuschem* 5 (2012) 2410–2420, <https://doi.org/10.1002/cssc.201200416>.
- [15] J.A. Lopez-Ruiz, E. Andrews, S.A. Akhade, M.S. Lee, K. Koh, U. Sanyal, S.F. Yuk, A. J. Karkamkar, M.A. Derewinski, J. Holladay, V.A. Glezakou, R. Rousseau, O. Y. Gutierrez, J.D. Holladay, Understanding the role of metal and molecular structure on the electrocatalytic hydrogenation of oxygenated organic compounds, *ACS Catal.* 9 (2019) 9964–9972, <https://doi.org/10.1021/acscatal.9b02921>.
- [16] Y. Song, S.H. Chia, U. Sanyal, O.Y. Gutierrez, J.A. Lercher, Integrated catalytic and electrocatalytic conversion of substituted phenols and diaryl ethers, *J. Catal.* 344 (2016) 263–272, <https://doi.org/10.1016/j.jcat.2016.09.030>.
- [17] L. Xin, Z.Y. Zhang, J. Qi, D.J. Chadderton, Y. Qiu, K.M. Warsko, W.Z. Li, Electricity storage in biofuels: selective electrocatalytic reduction of levulinic acid to valeric acid or gamma-valerolactone, *Chemsuschem* 6 (2013) 674–686, <https://doi.org/10.1002/cssc.201200765>.
- [18] J.A. Lopez-Ruiz, U. Sanyal, J. Egbert, O.Y. Gutierrez, J. Holladay, Kinetic investigation of the sustainable electrocatalytic hydrogenation of benzaldehyde on Pd/C: effect of electrolyte composition and half-cell potentials, *ACS Sustain. Chem. Eng.* 6 (2018) 16073–16085, <https://doi.org/10.1021/acssuschemeng.8b02637>.
- [19] X.H. Chadderton, D.J. Chadderton, T. Pfennig, B.H. Shanks, W.Z. Li, Paired electrocatalytic hydrogenation and oxidation of 5-(hydroxymethyl)furfural for efficient production of biomass-derived monomers, *Green Chem.* 21 (2019) 6210–6219, <https://doi.org/10.1039/C9GC02264C>.
- [20] X.H. Chadderton, D.J. Chadderton, J.E. Matthies, Y. Qiu, J.M. Carraher, J. P. Tessonier, W.Z. Li, Mechanisms of furfural reduction on metal electrodes: distinguishing pathways for selective hydrogenation of bioderived oxygenates, *J. Am. Chem. Soc.* 139 (2017) 14120–14128, <https://doi.org/10.1021/jacs.7b06331>.
- [21] Y. Song, U. Sanyal, D. Pangotra, J.D. Holladay, D.M. Camaioni, O.Y. Gutierrez, J. A. Lercher, Hydrogenation of benzaldehyde via electrocatalysis and thermal catalysis on carbon-supported metals, *J. Catal.* 359 (2018) 68–75, <https://doi.org/10.1016/j.jcat.2017.12.026>.
- [22] T.R. Dos Santos, F. Harnisch, P. Nilges, U. Schroder, Electrochemistry for biofuel generation: transformation of fatty acids and triglycerides to diesel-like olefin/ether mixtures and olefins, *Chemsuschem* 8 (2015) 886–893, <https://doi.org/10.1002/cssc.201403249>.
- [23] G. Yuan, C. Wu, G. Zeng, X. Niu, G. Shen, L. Wang, X. Zhang, R. Luque, Q. Wang, Kolbe electrolysis of biomass-derived fatty acids over Pt nanocrystals in an electrochemical cell, *ChemCatChem* 12 (2019) 642–648, <https://doi.org/10.1002/cctc.201901443>.
- [24] Y.M. Zhang, G.R. Liu, J.H. Wu, Electrochemical conversion of palmitic acid via Kolbe electrolysis for synthesis of n-triacontane, *J. Electroanal. Chem.* 822 (2018) 73–80, <https://doi.org/10.1016/j.jelechem.2018.05.018>.
- [25] P.F. Levy, J.E. Sanderson, R.G. Kispert, D.L. Wise, Biorefining of biomass to liquid fuels and organic-chemicals, *Enzym. Microb. Technol.* 3 (1981) 207–215, [https://doi.org/10.1016/0141-0229\(81\)90087-9](https://doi.org/10.1016/0141-0229(81)90087-9).
- [26] P.F. Levy, J.E. Sanderson, L.K. Cheng, Kolbe electrolysis of mixtures of aliphatic organic-acids, *J. Electrochem. Soc.* 131 (1984) 773–777, <https://doi.org/10.1149/1.2115697>.
- [27] P. Nilges, T.R. Dos Santos, F. Harnisch, U. Schröder, Electrochemistry for biofuel generation: electrochemical conversion of levulinic acid to octane, *Energy Environ. Sci.* 5 (2012) 5231–5235, <https://doi.org/10.1039/C1EE02685B>.
- [28] S. Palkovits, R. Palkovits, The role of electrochemistry in future dynamic biorefineries: a focus on (Non-)Kolbe electrolysis, *Chem. Ing. Tech.* 91 (2019) 699–706, <https://doi.org/10.1002/cite.201800205>.
- [29] C. Stang, F. Harnisch, The dilemma of supporting electrolytes for electroorganic synthesis: a case study on Kolbe electrolysis, *Chemsuschem* 9 (2016) 50–60, <https://doi.org/10.1002/cssc.201501407>.
- [30] H. Kolbe, Zersetzung der Valeriansäure durch den elektrischen Strom, *J. Liebigs Ann. Chem.* 64 (1848) 339–341.
- [31] T. Kunugi, Electrolytic oxidation of salts of aliphatic acids by the Hofer-Moest reaction 1. Formation of methanol from sodium acetate, *J. Am. Chem. Soc.* 75 (1953) 1597–1599, <https://doi.org/10.1021/ja01103a024>.
- [32] H.J. Schäfer, Recent contributions of kolbe electrolysis to organic synthesis, in: E. Steckhan (Ed.), *Electrochemistry IV. Topics in Current Chemistry*, vol 152, Springer, Berlin, Heidelberg, 1990.
- [33] Y. Peng, Y.Z. Ning, X.X. Ma, Y.S. Zhu, S. Yang, B. Su, K.S. Liu, L. Jiang, Bioinspired underwater superoleophobic electrodes with superior kolbe electrochemical performances, *Adv. Funct. Mater.* 28 (2018), 1800712, <https://doi.org/10.1002/adfm.201800712>.
- [34] Y. Qiu, J.A. Lopez-Ruiz, U. Sanyal, E. Andrews, O.Y. Gutierrez, J.D. Holladay, Anodic electrocatalytic conversion of carboxylic acids on thin films of RuO₂, IrO₂, and Pt, *Appl. Catal. B-Environ.* 277 (2020), 119277, <https://doi.org/10.1016/j.apcatb.2020.119277>.
- [35] J.A. Lopez-Ruiz, R.J. Davis, Decarbonylation of heptanoic acid over carbon-supported platinum nanoparticles, *Green Chem.* 16 (2014) 683–694, <https://doi.org/10.1039/C3GC41287C>.
- [36] G. Yuan, L. Wang, X.W. Zhang, R. Luque, Q.F. Wang, Core-shell Pt@Ir nanothorns on carbon fiber paper electrodes for carboxylic acid valorization via kolbe electrolysis, *ACS Sustain. Chem. Eng.* 7 (2019) 18061–18066, <https://doi.org/10.1021/acssuschemeng.9b05045>.

- [37] J.C. Cruz, V. Baglio, S. Siracusano, V. Antonucci, A.S. Aricò, R. Ornelas, L. Ortiz-Frade, G. Osorio-Monreal, S.M. Durón-Torres, L.G. Arriaga, Preparation and characterization of RuO₂ catalysts for oxygen evolution in a solid polymer electrolyte, *Int. J. Electrochem. Sci.* 6 (2011) 6607–6619.
- [38] Y. Qiu, J.J. Huo, F. Jia, B.H. Shanks, W.Z. Li, N- and S-doped mesoporous carbon as metal-free cathode catalysts for direct biorenewable alcohol fuel cells, *J. Mater. Chem. A* 4 (2016) 83–95, <https://doi.org/10.1039/C5TA06039G>.
- [39] Y. Qiu, L. Xin, F. Jia, J. Xie, W.Z. Li, Three-dimensional phosphorus-doped graphitic-C₃N₄ self-assembly with NH₂-functionalized carbon composite materials for enhanced oxygen reduction reaction, *Langmuir* 32 (2016) 12569–12578, <https://doi.org/10.1021/acs.langmuir.6b02498>.
- [40] Y. Qiu, L. Xin, W.Z. Li, Electrocatalytic oxygen evolution over supported small amorphous Ni-Fe nanoparticles in alkaline electrolyte, *Langmuir* 30 (2014) 7893–7901, <https://doi.org/10.1021/la501246e>.
- [41] S. Cherevko, S. Geiger, O. Kasian, N. Kulyk, J.P. Grote, A. Savan, B.R. Shrestha, S. Merzlikin, B. Breitbach, A. Ludwig, K.J.J. Mayrhofer, Oxygen and hydrogen evolution reactions on Ru, RuO₂, Ir, and IrO₂ thin film electrodes in acidic and alkaline electrolytes: a comparative study on activity and stability, *Catal. Today* 262 (2016) 170–180, <https://doi.org/10.1016/j.cattod.2015.08.014>.
- [42] Y. Qiu, L. Xin, D.J. Chadderton, J. Qi, C.H. Liang, W.Z. Li, Integrated electrocatalytic processing of levulinic acid and formic acid to produce biofuel intermediate valeric acid, *Green Chem.* 16 (2014) 1305–1315, <https://doi.org/10.1039/C3GC42254B>.
- [43] D.J. Morgan, Resolving ruthenium: XPS studies of common ruthenium materials, *Surf. Interface Anal.* 47 (2015) 1072–1079, <https://doi.org/10.1002/sia.5852>.
- [44] J. Zheng, S.Y. Zhou, S. Gu, B.J. Xu, Y.S. Yan, Size-dependent hydrogen oxidation and evolution activities on supported palladium nanoparticles in acid and base, *J. Electrochem. Soc.* 163 (2016) F499–F506, <https://doi.org/10.1149/2.0661606jes>.
- [45] N.T. Suen, S.F. Hung, Q. Quan, N. Zhang, Y.J. Xu, H.M. Chen, Electrocatalysis for the oxygen evolution reaction: recent development and future perspectives, *Chem. Soc. Rev.* 46 (2017) 337–365, <https://doi.org/10.1039/C6CS00328A>.
- [46] T. Shinagawa, A.T. Garcia-Esparza, K. Takanabe, K. Insight on Tafel slopes from a microkinetic analysis of aqueous electrocatalysis for energy conversion, *Sci. Rep.* 5 (2015) 13801, <https://doi.org/10.1038/srep13801>.
- [47] T. Reier, M. Oezaslan, P. Strasser, Electrocatalytic oxygen evolution reaction (OER) on Ru, Ir, and Pt catalysts: a comparative study of nanoparticles and bulk materials, *ACS Catal.* 2 (2012) 1765–1772, <https://doi.org/10.1021/cs3003098>.
- [48] S. Cherevko, N. Kulyk, K.J.J. Mayrhofer, Durability of platinum-based fuel cell electrocatalysts: dissolution of bulk and nanoscale platinum, *Nano Energy* 29 (2016) 275–298, <https://doi.org/10.1016/j.nanoen.2016.03.005>.
- [49] A. Damjanovic, V.I. Birss, D.S. Boudreaux, Electron-transfer through thin anodic oxide-films during the oxygen evolution reactions at Pt electrodes 1. Acid-solutions, *J. Electrochem. Soc.* 138 (1991) 2549–2555, <https://doi.org/10.1149/1.2086015>.